

An Image Analysis Program for Measuring Contact Angles of Arbitrary Drop Shape

F. Xia and P. Chen*

Department of Chemical Engineering, University of Waterloo, Waterloo, Ontario, Canada

Contact angle is important in the study of many industrial processes, involving wetting, such as ink jet printing, lithoplate, coating adhesion, and flotation. Numerous methodologies have been developed for the measurement of contact angles. But there still exist many problems; in particular, there is no good method available for measuring contact angles of irregular liquid drop shape. To overcome these difficulties, we developed a method, Contact Angle Measurement of Arbitrary Drop Shape (CAMADS), based on image analysis, with edge detection in sub-pixel resolution. Comparing with other methods, CAMADS has a good combination of features: simple, reliable, flexible, and reasonably precise, in measuring contact angles; it can be applied to situations of asymmetric drop shape. CAMADS was demonstrated by studying the *in vitro* wettability of hydrogel contact lenses, and superior, excellent results were obtained in comparison with other existing methods.

Journal of Imaging Science and Technology 47: 44–53 (2003)

Introduction

When a liquid is in contact with another fluid or solid, a contact angle is formed, and defined as the angle made between the two tangents aligned with the two surfaces of the media at the intersection point (Fig. 1). When the bottom medium is solid, we call the liquid drop a sessile drop. When the bottom medium is fluid, we call the liquid drop a liquid lens. The study of many industrial processes, involving wetting, including ink jet printing, lithoplate, coating adhesion, and flotation, requires knowledge of contact angles.^{1,2}

Numerous methodologies have been developed for the measurement of contact angles.^{3–6} Among them, direct measurement of contact angles from liquid drops or photographs of liquid drops is most widely used. In this technique, the angle is measured by aligning a tangent with the drop profile at the point of contact. The measurement can be performed either using a telescope equipped with a goniometer eyepiece, or on a photograph of the drop using a protractor. A precision of $\pm 2^\circ$ is usually claimed for this direct technique. However, aligning the tangent is subjective and dependent on the experience of the operator.

A more precise method for measuring contact angles is using the capillary rise at a vertical plate.^{6,7} The solid surface is brought into contact with the liquid, and the capillary rise at the vertical surface is measured. In addition to the capillary rise, the liquid surface tension, the density difference, and the gravitational acceleration

need to be known before the contact angle can be computed. The precision obtained with this technique is $\pm 0.1^\circ$, an order of magnitude better than the direct method. The disadvantage of this method is that large liquid volumes are required. And the configuration of a liquid lens cannot be employed because the capillary rise of a liquid at a solid surface is needed.

Two other precise techniques are interference microscopy and specular reflection.⁸ Interference microscopy relies on interference fringe patterns produced by the edge of the drop surface to calculate the contact angle. Specular reflection uses a beam of light reflected from the liquid surface. By pivoting the beam on its axis, the orientation at which the specular reflection disappears is determined, and the contact angle is established. The disadvantage of these two techniques is the use of sophisticated apparatus.

Another very important method is Axisymmetric Drop Shape Analysis-Profile⁹ (ADSA-P). The strategy employed to determine contact angles from the shapes of

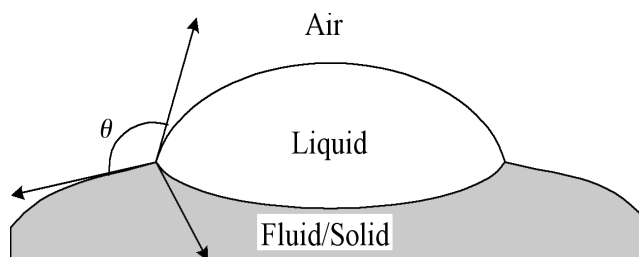


Figure 1. Schematic of the Contact Angle. When a liquid is in contact with another fluid or a solid surface, a contact angle is formed and defined as the angle made between the two tangents aligned with the two surfaces of the media at the intersection point.

Original manuscript received July 17, 2002

*Corresponding author, Tel: 1(519)888-4567x5586
Fax: 1(519)746-4979, email: p4chen@cape.uwaterloo.ca

©2003, IS&T—The Society for Imaging Science and Technology

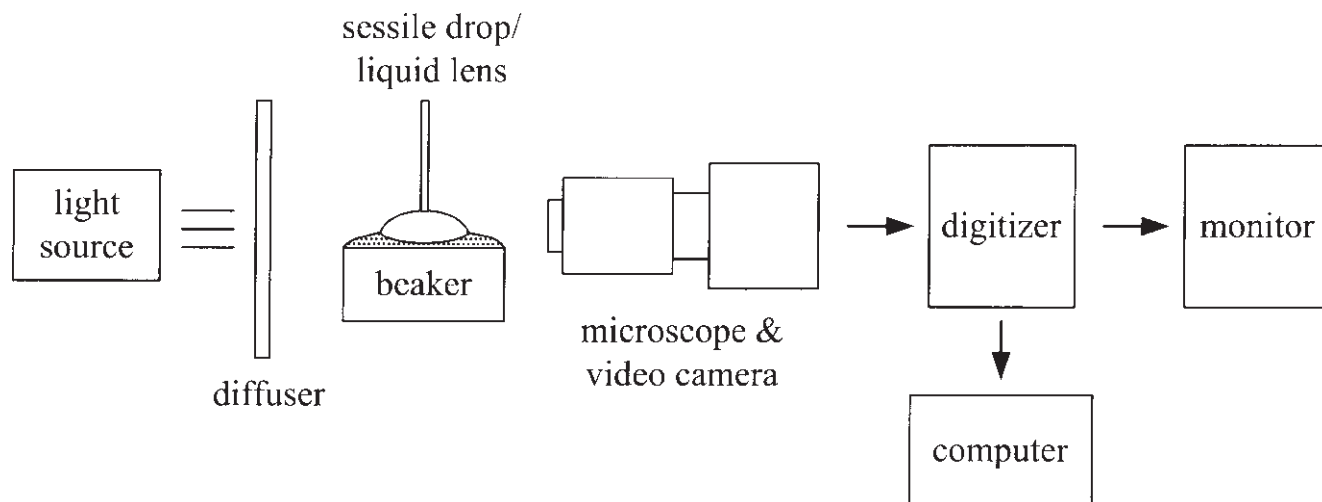


Figure 2. Schematic of an experimental setup for acquiring images of sessile drops/liquid lenses.

axisymmetric sessile drops is to construct an objective function which expresses the error between the physically observed and a theoretical Laplacian curve, i.e., a curve representing a solution to the Laplace equation of capillarity. This objective function is minimized numerically using the method of incremental loading in conjunction with the Newton-Raphson method. Contact angles can be computed as a fitting parameter with very high precision. But there are restrictions in using ADSA-P: regular drop shapes must be axisymmetric and the substrate solid surface must be flat.

An overview of these aforementioned techniques reveals that there are still many problems in contact angle measurement: using too sophisticated and expensive apparatus, lack of appropriate techniques for measuring irregular drop shapes such as a liquid lens, and large and uncontrollable errors brought by the operator. So it is very significant to develop a simple, objective, yet flexible method for measuring contact angles. To avoid using sophisticated and expensive apparatus, we focused our study on methods based on image analysis. To avoid the uncontrollable errors introduced by the operator, a computer image analysis algorithm and the corresponding software, Contact Angle Measurement of Arbitrary Drop Shape (CAMADS), were developed to generate drop profiles and calculate contact angles. With the sub-pixel resolution and advanced curve fit methods, CAMADS can measure contact angles of most regular and irregular drop shapes with high precision. With a batch-processing function, the user can calculate contact angles from a stack of drop images once initial parameters are given.

To demonstrate this new method, we apply it to measure the contact angles of care regimes on soft contact lenses. The reason for choosing the soft contact lenses is that the polymeric material of the lenses is similar to the many imaging materials, e.g., ink jet printing substrates, where surface roughness and heterogeneity, in addition to intrinsic polymer properties, are important factors in printing resolution and quality. On the other hand, these materials have been studied by various other methods. We can thus utilize the data generated by the existing methods and compare them with CAMADS. As will be shown, in the experiments of the contact angle measurement, the regime drop shapes were asymmetric and the quality of the drop images was

sometimes poor. Most of the existing image analysis based methods could not process all the drop images satisfactorily; part of the reason is due to the irregular shape of the drop. Here, we show CAMADS is capable of analyzing all images of irregular shape, and meaningful results can be obtained on wettability for a variety of combinations of hydrogel contact lenses and commercially available care regimes.

Algorithms and Methodologies

Since CAMADS is based on analyzing liquid drop images, image acquisition is performed first. An image analysis scheme is then applied to generate drop profiles: The edge detection is used as the first step, and a program follows to search the drop edge. To increase the precision of the coordinates of the searched edge points, the sub-pixel resolution with the natural spline curve fit method¹⁰ is applied to drop edge detection. Using the resulting coordinates, the intersection point at which surfaces and interfaces meet can be found by using an algebraic method (see later). Finally, the contact angle at the intersection point can be calculated by applying one of several curve fit methods, e.g., the polynomial with different degrees, to the detected edges.

The profile curve fit method is to minimize an objective function in the optimization scheme, which is a measure of the discrepancy between the calculated theoretic curve and the experimental data points. This objective function is the sum of the squares of the distance between the measured points and the calculated curve. The drop profile, thus, can be measured from the minimization of the objective function; this requires solving numerically a system of linear or non-linear algebraic equations.

Image Acquisition

Figure 2 shows a common experimental setup.¹¹ A sessile drop/liquid lens is illuminated with a white light source, shining through a heavily frosted glass diffuser. The image of the cross section of the sessile drop/liquid lens is obtained by a microscope linked to a monochrome charge-coupled device video camera. The video signal of the drop is transmitted to a digital video processor that performs the frame grabbing and digitization of the image to 640×480 pixels with 256 gray levels. A com-

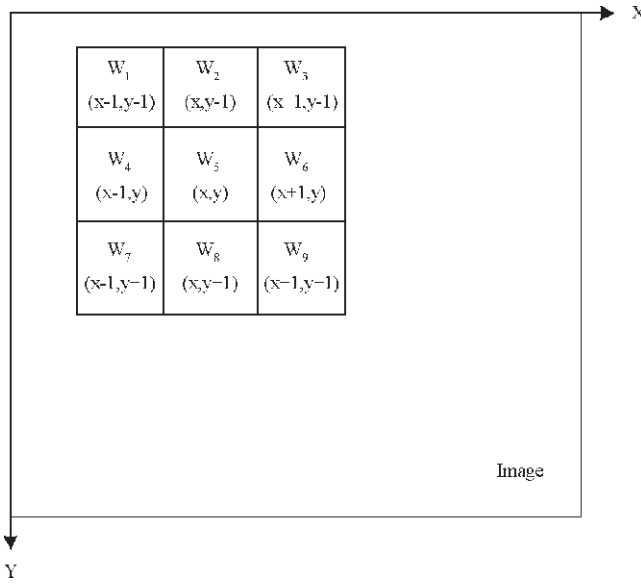


Figure 3. Rectangular subimage area with a 3×3 mask on pixel (x,y) . The coefficients of the mask are chosen to detect the gray level in the image. The center of the mask is moved around the image. At each pixel position in the image, we multiply the gray level of every pixel that is contained within the mask area by the corresponding mask coefficient. The results of these nine multiplications are then summed to approximate the gradient of (x,y) .

puter is used to store the images from the digitization board. The entire setup, except for the computer, is placed on a vibration-free table to isolate the system from external disturbances.

Edge Detection

After we acquire the drop image, an image analysis scheme is applied to extract the drop profile and to obtain the profile coordinates of the interfaces connected at the multiphase contact line. An edge is defined as the boundary (interface) between two regions with relatively distinct gray levels. The basic idea underlying most edge detection techniques is the computation of a local derivative operator.¹² Edge operators are based on the use of so-called convolution masks. A mask is a small, e.g., 2×2 or 3×3 , two-dimensional array, whose coefficients are chosen to detect a given property in an image (Fig. 3). The center of the mask is moved around the image. At each pixel position in the image, we multiply the gray level of every pixel that is contained within the mask area by a corresponding mask coefficient. The results of these nine multiplications are then summed and compared to approximate the gradient of the pixel position. The orientation of the edge can be treated as the direction with the corresponding maximal gradient (Fig. 4). For example, the gradient at E is calculated as

$$\text{gradient}(E) = \max \left[\begin{aligned} & \left| \left((gl(D) + 2 \times gl(A) + gl(B)) - (gl(F) + 2 \times gl(I) - gl(H)) \right) / 4 \right|, \\ & \left| \left((gl(A) + 2 \times gl(B) + gl(C)) - (gl(G) + 2 \times gl(H) - gl(I)) \right) / 4 \right|, \\ & \left| \left((gl(B) + 2 \times gl(C) + gl(F)) - (gl(D) + 2 \times gl(G) - gl(H)) \right) / 4 \right|, \\ & \left| \left((gl(C) + 2 \times gl(F) + gl(I)) - (gl(A) + 2 \times gl(D) - gl(G)) \right) / 4 \right| \end{aligned} \right] \quad (1)$$

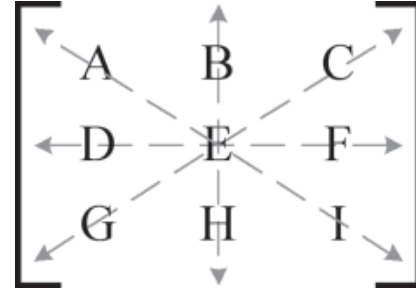


Figure 4. Four possible directions in which the change of the gray level of a pixel may occur for a 3×3 array.

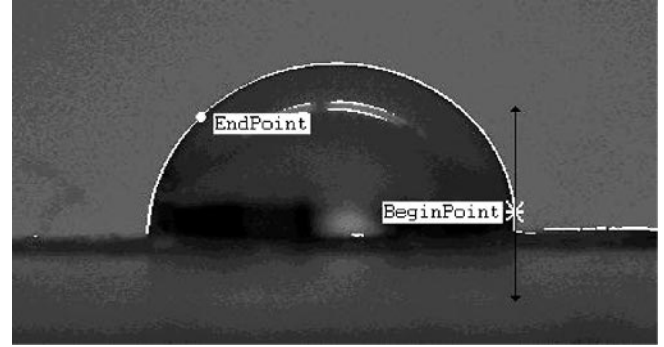


Figure 5. *Begin Point* and *End Point* are located on the drop profile for searching the profile between them. *Begin Point* is denoted by a star and *End Point* is denoted by a pie. At the *Begin Point*, there are two possible directions to search its next neighboring point. One is upward, and the other is downward.

where gl means the gray level. We adopt this edge operator because it has four possible orientations of the edge and it will be convenient to refine the edge by searching drop profiles and selecting pixels in those directions.

To extract and view the drop profile, one of the methods is by thresholding the output of the edge operator. If the output of the edge operator at a pixel exceeds a certain threshold, that pixel is determined to be a drop profile coordinate. It is noticed that the threshold will determine the “width” of the edge displayed; the greater the threshold is, the thinner the “width” will be.

Search the Drop Profile

After extracting the edge profile, the located drop profile coordinates may be several pixels wide because it is difficult to find a suitable threshold. One way to obtain a one-pixel-wide edge profile is to follow the local maxima of the operator output and find the drop edge profile coordinates. The procedure used in this study is as follows:

After two points, the *Begin* and *End Points*, are chosen on the edge profile (Fig. 5), the program will start from the *Begin Point* and search its neighboring edge pixels. Since a drop’s profile is smooth in nature, a compass directional search method¹⁵ can be used. Figure 6 shows one compass direction for a 3×3 mask on the current pixel E . The solid line represents the direction of the edge, which can be known when the edge detection is completed. Because the edge is assumed to be continuous, we only check the pixels in and near the edge direction, which means that the pixels B and H in Fig. 6 will not be checked as these two pixels are located in the normal direction. The dotted arrow line

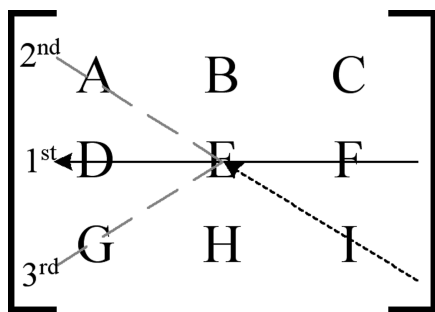


Figure 6. Search for a neighboring point of pixel *E* according to the edge direction *DEF* and the running direction *IE*. Pixel *D* is checked first, then pixel *A*, and finally pixel *G*.

represents the running direction in which the current pixel *E* comes from the last edge pixel *I*. Because the running direction is from *I* to *E* and the profile is continuous, the edge direction should go from *E* to *D*, not from *E* to *F*. The pixels *A*, *D* and *G* will be checked since they are the nearest pixels in the direction from *E* to *D*.

When starting from the *Begin Point*, the running direction is unknown because the *Begin Point* is the first point and has no previous edge pixel. It is impossible to ascertain the initial searching direction. Figure 5 shows that there are two possible opposite directions at the *Begin Point* for searching the next edge pixel. Thus, the initial running direction must be chosen by the user. Figure 7 shows the dialog for the user to select an initial running direction. The initial direction is an approximate direction; the user can select one from three possible directions, within an angle of $\pm 45^\circ$.

Once the edge direction and the running direction are known, three pixels, *D*, *A* and *G* (Fig. 6), will be checked as the next possible edge pixels. The gradient of pixel *D* will be checked first because it is located in the edge direction. Then the gradients of pixels *A* and *G* will be checked. Because pixel *A* is located in the extension of the running direction, pixel *A* will be checked before pixel *G*. The pixel that has the maximum gradient among pixels *D*, *A* and *G* will be chosen as the next edge pixel. Moving a 3×3 mask to the next edge pixel and continuing the search until the *End Point* is reached, all drop profile coordinates between the *Begin Point* and the *End Point* can be extracted from the images.

It is noted that there is no need for the maximum gradient to be greater than the threshold in searching the drop profile. While the edge displayed after the edge detection may be discontinuous because a large threshold has been selected, the search of the drop profile can still be performed using this algorithm. However, if the image is very blurry or the edge changes sharply, this algorithm may fail in achieving correct neighboring points because the information about the edge direction and the running direction may be disoriented.

Sub-pixel Resolution

In most studies, the edge detection scheme has only pixel resolution,¹¹ which results in a degree of uncertainty in edge profiles and further in contact angle values. Figure 8 shows a profile of part of the curve corresponding to an interface. It is seen that several steps occur. The error in each drop profile coordinate may be expected to be 1 to 2 pixels. For a sessile drop of 5 mm in diameter, this corresponds to an error of 25 μm

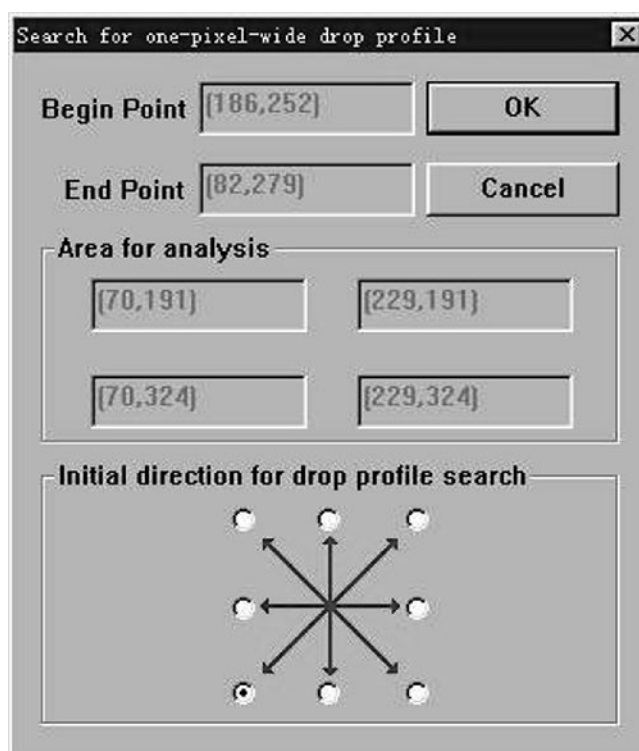


Figure 7. Dialogue to select the initial direction for searching a neighboring point at *Begin Point*. The initial direction is just an approximate direction. The user can select one from eight optional directions.

to 50 μm . One way to increase the precision is through the application of a sub-pixel resolution scheme.¹⁰

Figure 9 shows a typical example of the gradient profile approximately perpendicular to a drop interface. Point 5 is the pixel that was originally selected as the drop profile coordinate using the edge detection operator. It is clear that the gradient values near the edge start increasing gradually a few pixels away from the edge and decrease as we move past the edge. To refine the location of the edge to sub-pixel resolution, i.e., real or floating point coordinate values, different approaches can be used. Usually a curve is fitted to the gradient values of a few pixels in the direction normal to the edge, and the location with the maximum gradient value of the fitted curve is treated as the real edge point. It has been shown that the natural spline curve fit method is the most suitable for improving the precision.¹⁰ Comparing with polynomial curve fit methods, the natural spline curve passes through all of the data points while maintaining a smooth profile (Fig. 10). This means that the residual error is zero.¹³ On the other hand, because of the plateau on both sides of the gradient profile across the interface and the sudden increase and decrease in gradients at the interface, the polynomials will show large deviations from the original data. Therefore, we adopted the spline curve fit in CAMADS to find the maximum on the theoretical fitted curve. Figure 10 shows that a more precise edge point is located at 4.670314 after the natural spline curve fitting.

The application of sub-pixel resolution can be summarized as follows:

1. Select a pixel on the edge profile after edge detection.
2. Along the direction of the maximum gradient value, i.e., normal to the edge, select a number of pixels to use for the natural spline curve fitting.¹⁴

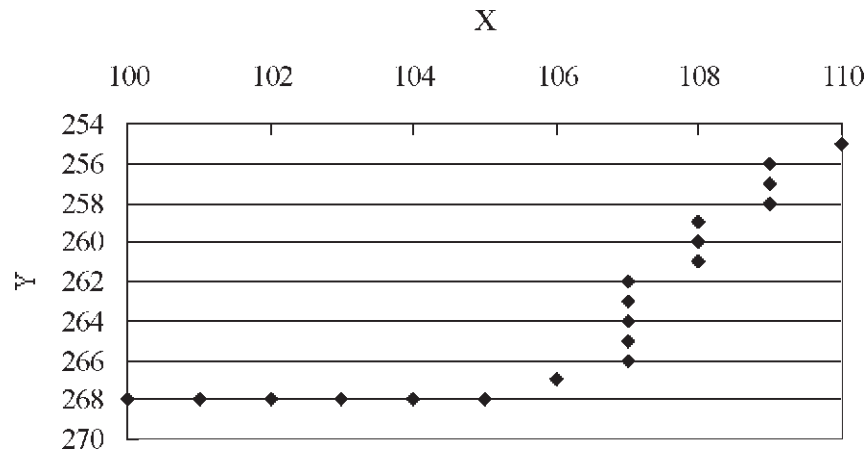


Figure 8. A drop profile acquired through the edge detection scheme with pixel resolution. Three steps occur in the lower portion of the curve because of the limitation of pixel resolution.

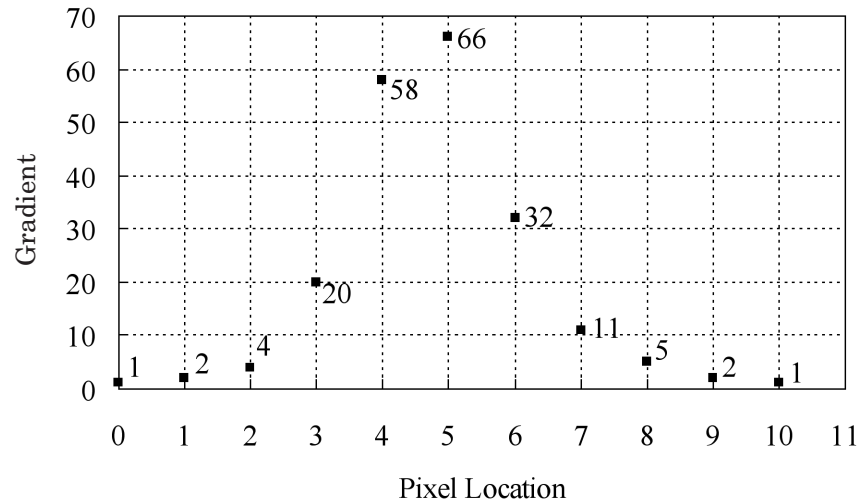


Figure 9. A gradient profile perpendicular to the drop interface. The values reach a maximum at the pixel location $p = 5$.

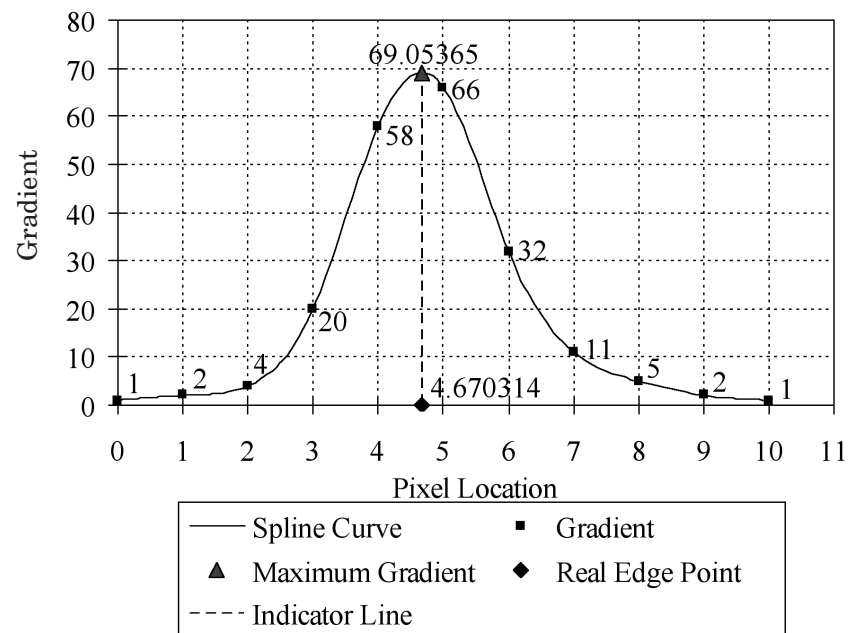


Figure 10. The intensity or gray level of the pixel changes across the edge of the drop. The gradient values reach a maximum at the pixel location that corresponds to the edge of the drop at $p = 5$. After refining the location of the edge to sub-pixel resolution, the real edge point is located at $p = 4.670314$ with the maximum gradient 69.05365° , indicated by the indicator line.

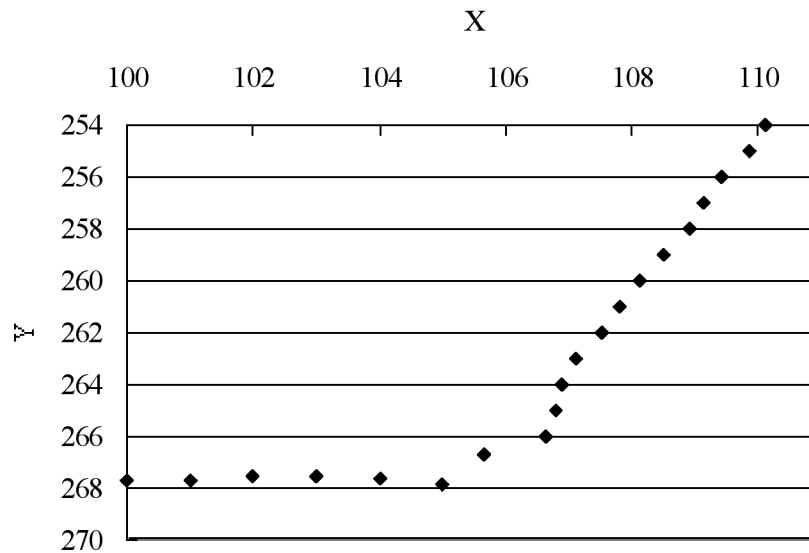


Figure 11. A drop profile acquired through the edge detection scheme with sub-pixel resolution.

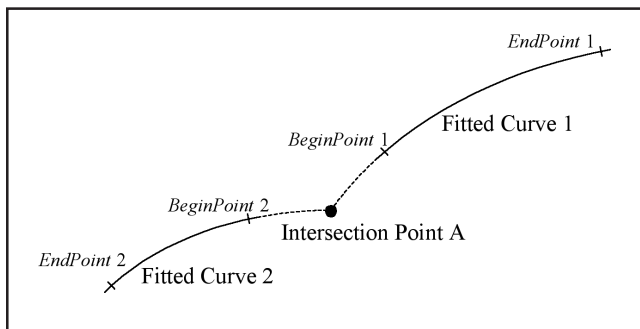


Figure 12. Illustration of the procedure for locating the intersection point A and calculating the contact angle: fitting two profile portions and computing the simultaneous solution to the two fitted equations.

3. Find the maximum gradient value from the fitted spline curve.

The outcome of this algorithm is shown in Fig. 11. From Fig. 11, it can be seen that, with sub-pixel resolution edge detection, rather smooth interfaces are obtained for the same drop profile in Fig. 8. The interfaces, which have real (or floating point) coordinate values, are more precise than those in Fig. 8.

Intersection Point and Contact Angle Calculation

After the edge detection and sub-pixel resolution have been obtained, the next step of the image analysis is to find the intersection point from the edge profile that has real (or floating point) coordinate values. The strategy is as follows: First, select two portions of the profile with a clear edge by locating four end points, in which the *Begin Points* of the liquid drop profile portions are selected as close as possible to the intersection point A (say, less than 10 points) (seen in Fig. 12). Then, perform curve fitting on each selected profile portion. The coordinates of the intersection point A are computed as the solution of simultaneous equations of the two fitted curves. Finally, the contact angle can be calculated as

the difference in slope between the two fitted curves at point A.

The curve fit methods adopted in CAMADS are the polynomials with different degrees from one to seven. Different methods have different advantages. The goodness-of-fit of polynomial curve fit methods depends on the degree of polynomials, the number and the type of data points.¹³ Normally, with the increase in degree and the decrease in number of data points, the residual errors of the curve fit methods decrease. If the data points do not actually lie on a polynomial curve, then the least squares polynomials may exhibit large oscillations.¹⁵ This phenomenon, called *polynomial wiggle*, becomes more pronounced with higher degree polynomials (Fig. 13). Hence we should seldom use a polynomial of degree 6 or above unless it is known that the true function we are working with is such a polynomial.

For a nearly straight line profile, the linear curve fit method is the best choice. For a clearly curved profile, the linear curve fit method is obviously unsuitable. For a liquid drop surface profile that is clearly curved, we know the best curve fit method is to use the Laplacian equation of capillarity to fit the drop profile, which is adopted in ADSA-P.⁹ When using polynomials to fit the drop boundary points, the residual errors are calculated as the standard deviation in y-direction with the distance between two neighboring pixels as the unit. From the residual error distribution function plot (Fig. 14), we see that in a range of fitting points (from 8 to 190), the residual error of the cubic curve fit method is small (below 0.3). It means that the cubic curve provides a well fitted representation of the data. On the other hand, if the portion of a drop profile near the intersection point can be fitted very well, even if the fitted curve may show large deviation at the portion of the drop profile far from the intersection point, the contact angle at the intersection point can still be calculated rather precisely. When using CAMADS, we have no need to fit a whole drop profile. Usually the portion of the drop profile to be fitted contains enough well-distributed data points, about 100 nearly equally spaced pixels, and its second derivative keeps the same sign, which avoids fluctuation in data points. In addition, the intersection point to be extrapolated is very close to the *Begin Point* of the portion of the drop profile (less than 10 pixels). The cu-

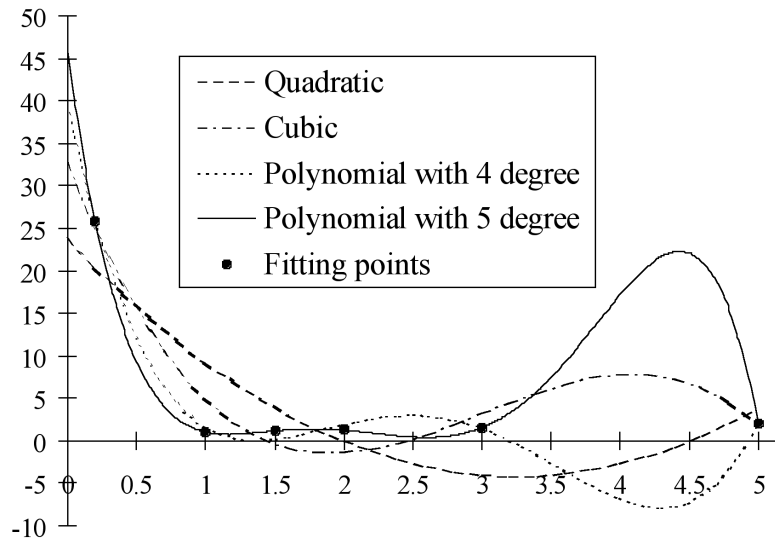


Figure 13. The phenomenon of “polynomial wiggle”. The six data points are generated by the function $f(x) = x^{-2} + \sqrt{1x - 1}$ on 0.2, 1, 1.5, 2, 3, and 5. The least squares polynomials $P_4(x)$ and $P_5(x)$ exhibit a large wiggle in the interval.^{3,5} Indeed, $P_5(x)$ goes through the six data points and it is the worst approximation. If we had to use a polynomial, then $P_2(x)$ or $P_3(x)$ should be our choice.

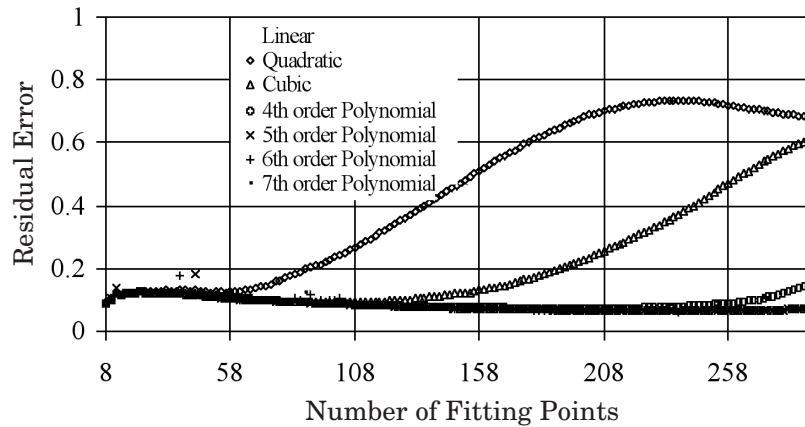


Figure 14. Residual error distribution function plot for different polynomials with degrees from 1 to 6, fitting on the drop boundary points. The number of the data points varies from 8 to 293. The residual error is calculated on the coordinates of a curved drop profile with a contact angle approximately 45° . In a range of fitting points (from 8 to 190), the residual error of the cubic fit method is very small (below 0.3).

bic curve fit method can be applied to a simple curve and be extrapolated to an intersection point. The angles calculated by it will not be influenced greatly by a few points near the intersection point.

Application to Contact Angle Measurement of Soft Contact Lenses

In this demonstration, CAMADS was employed to study the wettability for a variety of combinations of hydrogel polymers and commercially available care regimens. The experiment involved the use of four care regimens (Table I) and five contact lens materials (Table II) for 20 possible combinations.

To quantify the wettability of the four solutions on the hydrated surfaces of the five soft contact lenses, a contact angle measurement technique was needed. Because the storage solution and the solutions to be studied were completely miscible, it proved impossible to form stable liquid drops on such wet surfaces.¹⁶ In addition, the lenses were soft and curved; thus the sessile drop experiments could not be performed in the com-

monly undertaken manner, and a novel sample preparation approach was devised: A lens (diameter 14 mm) was initially cut into four small pieces, each of which was used as a sample. This sample was placed on the flat surface of a sample stand made of Teflon. Because the sample was small in size and completely wet, it became flat and adhered to the surface of the stand. By using a paper tissue to remove excess liquid on the surface of the sample, the surface became “semi-dry”. A drop of the liquid to be studied was manually dispensed on the sample surface while simultaneously acquiring an image stack, recording the spreading process, using a software package (UTHSCSA *ImageTool for Windows 2.00*). Each image stack contained 100 single images. The time interval between two images was 0.1 ~ 0.3 seconds, providing up to 300 images per stack. By using CAMADS, each image in the stack could be analyzed. For each contact angle measurement, about ten image stacks were captured (Fig. 15).

Table III summarizes the results of the contact angles for all combinations. From Table III, we may see large

TABLE I. Four Care Regimes

Solutions	Contents
CIBA-Vision AOSep TM	A sterile ophthalmic solution containing micro-filtered hydrogen peroxide (3%) (w/v), sodium chloride 0.85% (w/v), stabilized with phosphonic acid and buffered with phosphates.
Allergan Complete Comfort Plus TM	Buffer: phosphate Surfactant: Poloxamine 237 Lubricant: HPMC (hydroxypropyl methylcellulose) Preservative: PHMB (polyaminopropyl biguanide 0.0001%)
Alcon Optifree Express TM	Buffer: phosphate Lubricant: HPMC (hydroxypropyl methylcellulose) Disinfectant/Preservative: PHMB (polyaminopropyl biguanide 0.0001%)
Bausch and Lomb ReNu MultiPlus TM	DYMED: (polyaminopropyl biguanide) 0.0001% Edetate Disodium 0.10% HYDRANATE: (hydroxyalkylphosphonate) Poloxamine Boric Acid, sodium chloride and sodium borate

TABLE II. Five Contact Lenses and Materials

Proprietary Name	Manufacturer	Ct (@-3.00D) mm	Water Content	Dk	Dk/tx	FDA 10°@35°C	USAN Group
PureVision TM	Bausch and Lomb	0.09	36%	99	110	III	Balafilcon A
Focus Night&Day TM	CIBA-Vision	0.08	24%	140	175	I	Lotrafilcon A
Proclear TM	Biocompatibles	0.065	62%	25.6	39.3	II	Omafilcon A
Optima 38 TM	Bausch and Lomb	0.035	38%	9.5	27.2	I	Polymacon
Acuvue TM	Vistakon	0.07	58%	21.7	31.0	IV	Etafilcon A

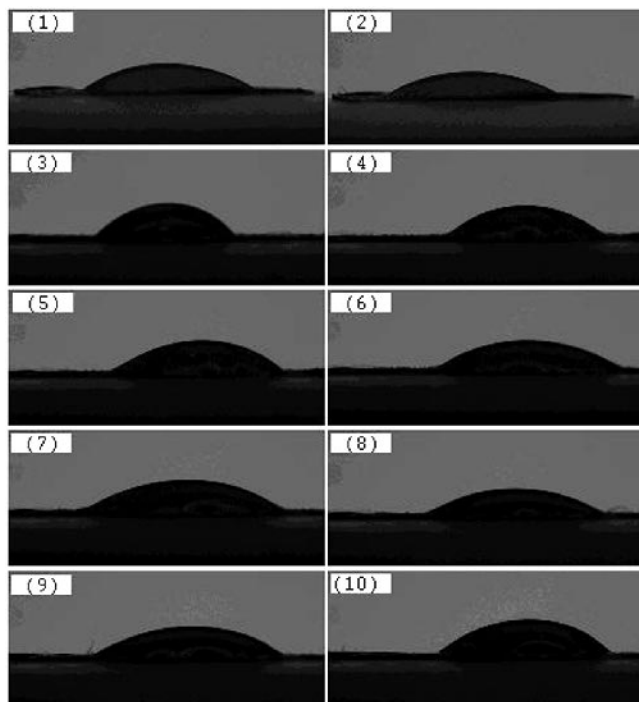


Figure 15. Ten image stacks of ReNu MultiPlusTM on PureVisionTM. Only the last image of each stack was analyzed and shown here because it contained the most stable drop comparing with the earlier images in that stack.

standard errors in some cases. This is due to the poor reproducibility of the experiments. For example, the mean contact angle of ReNu MultiPlusTM on PureVisionTM is 33.8814°, with a large standard error 5.0679°. If we observe the drop images in Fig. 15, which are used to mea-

sure the contact angles of ReNu MultiPlusTM on PureVision, we can see that the ten experimental drop images are quite different. The drops (3) and (10) are obviously more curved than the others; and the drop (2) is obviously flatter than the others. Because we could not obtain the same drop images when repeating the experiments of the same regimes on the same contact lenses, large standard errors resulted when calculating contact angles statistically on a group of different drops.

Figure 16 graphically illustrates the results of the contact angles for all combinations and provides a useful means of discussion of the results. Figure 16(a) reveals clear trends, the most obvious being that regardless of care regime, the order of *in vitro* wettability (greatest to least) was AcuvueTM, OptimaTM, ProclearTM, Focus Night&DayTM, and PureVisionTM. This indicates that currently available contact lens polymers exhibit a variety of significant *in vitro* wetting angles. Figure 16(b) reveals the wettability of the four solutions is sorted from the lowest to the highest as: AOSepTM, CompleteTM, OptiFree ExpressTM, and ReNu MultiPlusTM. This indicates that currently available contact lens solutions provide differing wetting surfaces to hydrogels.

Comparison between Three Contact Angle Measurement Methods

When studying the *in vitro* wettability of hydrogel contact lenses, three methods were used to analyze the contact angles of four care regimes on five soft contact lenses. The first method was CAMADS, the second was ADSA-P, and the third was a manual measurement. The procedure for the use of ADSA-P is as follows: For a drop image, the necessary parameters, e.g., the density of the solutions, the gravitational acceleration, and the coordinates of the intersection points, are input into a text file. Then a program is run in MS-DOS to apply the edge detection, sub-pixel resolution and Laplacian curve fitting. Finally the contact angle results are found in an output text file. The manual measurement

TABLE III. Experimental results of contact angles of the four solutions on the five contact lenses by using CAMADS. The average contact angles and the standard errors were calculated based on each group.

Contact Lenses	Solutions			
	AOSpet™	Complete™	Express™	MultiPlus™
PureVision™	75.9388±3.2604	47.9419±1.6453	37.2359±1.5850	33.8814±5.0679
Focus™	55.3645±1.0412	27.7172±4.2222	14.6303±1.4380	15.7129±2.4389
Proclear™	19.7895±3.5337	19.5627±3.3178	13.1501±2.5144	11.9605±3.6217
Optima™	19.2256±3.9274	15.9898±1.3146	11.0357±3.9540	15.2678±1.7856
Acuvue™	15.5351±3.5568	10.5447±1.8824	11.7167±1.7964	9.6064±3.6187

TABLE IV. Comparison results between manual measurement and CAMADS. A drop image of ReNu MultiPlus™ on PureVision™ was analyzed 14 times repeatedly by the manual measurement and CAMADS, respectively. When CAMADS was used, the linear curve fit method was employed on the solid surface profile, the cubic curve fit method was employed on the liquid drop surface profile. If the input of CAMADS are the same, the results of CAMADS are the same, without errors brought by the operator.

Contact Angle of ReNu MultiPlus™ on PureVision™								Average	Std. Err.
Manual Measurement	33.25	29.38	30.82	27.5	24.98	29.5	27.16	29.31143	3.304735
	26.82	31.59	29.49	25.4	30.04	27.05	37.38		
CAMADS	29.88	29.88	29.88	29.88	29.88	29.88	29.88	29.88	
	29.88	29.88	29.88	29.88	29.88	29.88	29.88		

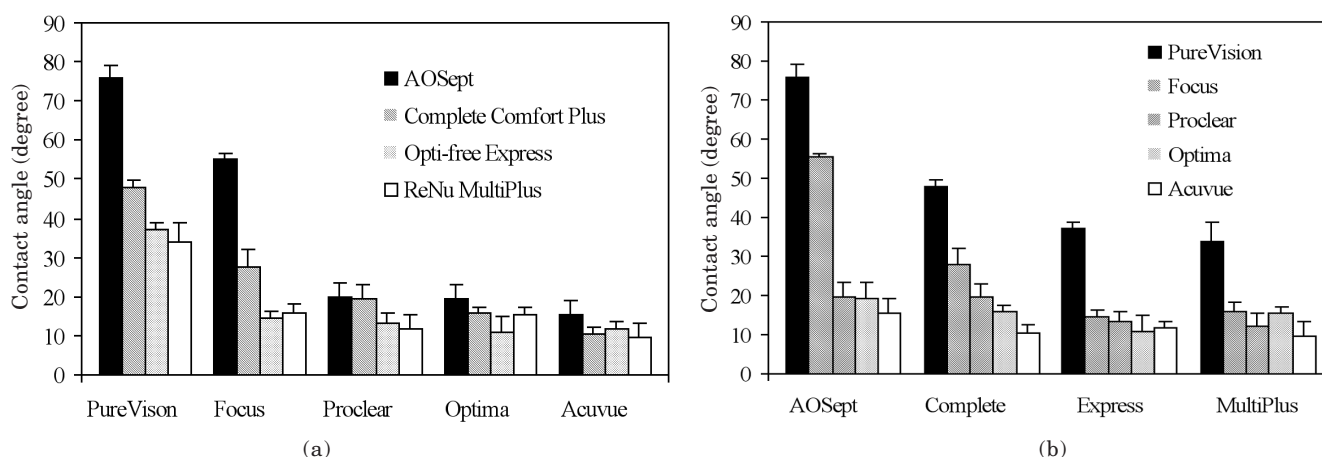


Figure 16. Results of contact angles of four solutions on five contact lenses by using CAMADS. From Fig. 16(a), the wettability of the five contact lenses can be identified from the lowest to the highest in the following order: PureVision™, Focus Night&Day™, Proclear™, Optima 38™, and Acuvue™. From Fig. 16(b), the wettability of the four solutions on the five contact lenses can be identified from the lowest to the highest in the following order: AOSep™, Complete™, OptiFree Express™, and ReNu MultiPlus™.

is as follows: For a drop image opened by the software *ImageTool 2.0*, the user draws two straight lines from a point predetermined by the user as the intersection point. Then the angle between the two straight lines is calculated as the contact angle by the software *ImageTool 2.0*.

Table IV shows the comparison between CAMADS and the manual measurement, in which the average contact angles of the two measurements are close. It is seen in Table IV that when manually measuring contact angles, the standard error brought by the operator is large. But if employing CAMADS, the results are repeatable. It means that the results in the manual measurement are not entirely objective and human errors are involved in the measurement.

Table V shows the comparison between CAMADS and ADSA-P. Fifteen images were analyzed. When using CAMADS, left and right angles were measured separately. For those images whose left and right contact

angles are very close, they can be treated as axisymmetric drops for ADSA-P. For those images whose left and right contact angles are widely different (say, larger than $\pm 5^\circ$), the drops have to be treated as non-axisymmetric drops. For those axisymmetric drops, the errors between the results of ADSA-P and CAMADS are very small, with the deviation of less than 5%. These small discrepancies can be explained by the following differences:

1. ADSA-P analyzes the whole drop profile assuming that the solid surface is ideal and the liquid drop is axisymmetric; in reality, neither of these can be exactly true. In contrast, CAMADS only considers the area near the contact point and measures the local contact angle. Thus, for a real surface the results of ADSA-P and CAMADS should be different.
2. A polynomial used in CAMADS is not a perfect function to describe drop profiles. The governing equation is the Laplacian equation.

TABLE V. Comparison results between ADSA-P and CAMADS. The drops of four care regimes on five contact lenses were produced repeatedly. When the drop shapes became stable, the contact angles were measured. When CAMADS was used, the linear curve fit method was employed on the solid surface profile and the cubic curve fit method was employed on the liquid drop surface profile. The drops, whose left and right contact angles were very close, could be regarded as axisymmetric drops that meet the requirement of ADSA-P.

ADSA-P				CAMADS			
Axisymmetric Angle (AA)	Left Angle (LA)	AA-LA	$\frac{ AA-LA }{AA}$	Right Angle (RA)	AA-RA	$\frac{ AA-RA }{AA}$	LA-RA
86.7793	83.3378	3.4416	0.0397	80.0559	6.7234	0.0775	3.2819
FAILED	79.1306			79.3958			0.2652
71.9675	68.3434	3.6241	0.0504	65.3802	6.5873	0.0915	2.9632
54.4164	52.7203	1.6961	0.0312	50.6489	3.7675	0.0692	2.0714
51.2193	48.1852	3.0341	0.0592	53.1733	1.9540	0.0381	4.9881
FAILED	47.7014			44.6943			3.0071
45.3816	46.5566	1.1750	0.0259	42.3727	3.0089	0.0663	4.1839
42.8581	44.6676	1.8095	0.0422	47.2521	4.3940	0.1025	2.5845
39.8525	39.8798	0.0273	0.0007	38.2761	1.5764	0.0396	1.6037
FAILED	37.5907			31.4533			6.1374
33.1976	37.0662	3.8686	0.1165	29.2306	3.9670	0.1195	7.8356
36.3740	35.9620	0.4120	0.0113	35.9736	0.4004	0.0110	0.0116
32.4082	33.0807	0.6725	0.0208	32.0737	0.3345	0.0103	1.007
33.7779	29.9562	3.8217	0.1131	43.2097	9.4318	0.2792	13.2535
29.6881	29.8907	0.2026	0.0068	27.5611	2.1270	0.0716	2.3296

For those non-axisymmetric images, the requirements of ADSA-P cannot be met. So ADSA-P is not applicable and the resulting angles of ADSA-P are erroneous.

Furthermore, there are some images that ADSA-P could not deal with but CAMADS could, even though the drops could be regarded as axisymmetric. This fact shows the robustness of CAMADS, and the limitation of ADSA-P's algorithm. ADSA-P uses the Newton-Raphson method^{9,17} combining the method of incremental loading^{9,17} to solve a set of nonlinear algebraic equations. The major disadvantage of this algorithm is the convergence. If poor initial values are used, the algorithm may fail to achieve a solution. Consequently, even though some drops were axisymmetric, ADSA-P still failed to analyze them. But using CAMADS, the user can always analyze them and obtain appropriate results because CAMADS does not involve iterative differential equation solutions.


Conclusions

To measure contact angles from sessile drops and liquid lenses of arbitrary drop shape, we developed a new computer program, Contact Angle Measurement of Arbitrary Drop Shape (CAMADS), based on image analysis. The algorithms in the program execute the following:

1. For a drop image, the edge profile is extracted by applying edge detection. A sub-pixel resolution scheme is employed, where the natural spline curve fit method is adopted, in order to increase the precision of the coordinates of the profile.
2. The intersection point and the contact angle are calculated by solving two algebraic equations of the fitted curves to two intersecting profile portions.

Comparing with other methods, CAMADS has a good combination of features: simple, reliable, flexible, and reasonably precise, in measuring contact angles; it can be applied to situations of asymmetric drop shape.

When studying the *in vitro* wettability of hydrogel contact lenses, CAMADS succeeded in identifying the wettability of four solutions on five contact lenses. The results show that currently available contact lens polymers exhibit a variety of significant *in vitro* wetting

angles, and that currently available contact lens solutions provide differing wetting surfaces to hydrogels. However, these conclusions cannot be drawn readily with other existing contact angle measurement methods. 

Acknowledgment. The financial support of this research was provided by the Natural Sciences and Engineering Research Council of Canada (NSERC). We thank John Long of the Department of Chemical Engineering, University of Waterloo, and Lyndon Jones of the Centre for Contact Lens Research, School of Optometry, University of Waterloo for the contact lens experiments and useful discussions.

References

1. A. W. Neumann, D. R. Absolom, D. W. Francis, S. N. Omenyi, J. K. Spelt, Z. Policova, C. Thomson, W. Zingg, and C. J. van Oss, *Ann. New York Acad. Sci.* **276**, 416 (1983).
2. A. W. Neumann, D. R. Absolom, W. Zingg, C. J. van Oss, and D. W. Francis, in *Biocompatible Polymers, Metals & Composites*, M. Szycher, Ed., Technomic Publishing Co. Lancaster, PA, 1983, p. 53.
3. J. F. Padday, in *Surface and Colloid Science*, vol. 1, E. Matijevic, Ed., Wiley, New York, 1969, p. 101.
4. D. S. Ambwani and Jr. T. Fort, in *Experimental Methods in Surface and Colloid Science*, vol. 11, R. J. Good and R. R. Stromberg, Eds., Plenum Press, New York, 1979, p. 93.
5. A. W. Adamson, *Physical Chemistry of Surfaces*, 5th ed., Wiley, New York, 1990.
6. A. W. Neumann and R. J. Good, in Ref. 4, p. 31.
7. A. W. Neumann, *Adv. Colloid Interface Sci.* **105**, 4 (1974).
8. C. Allain, D. Ausserre and F. Rondelez, *J. Colloid Interface Sci.* **107**, 5 (1985).
9. Y. Rotenberg, L. Boruvka and A. W. Neumann, *J. Colloid Interface Sci.* **93**, 169 (1983).
10. P. W. P. Cheng, Automation of Axisymmetric Drop Shape Analysis Using Digital Image Processing, Ph.D. Thesis, University of Toronto, 1990.
11. P. Chen, S. S. Susnar, A. Amirfazi, C. Mak, and A. W. Neumann, *Langmuir* **13**, 3035 (1997).
12. R. C. Gonzalez and P. Wintz, *Digital Image Processing*, 2nd ed., Addison-Wesley, New York, 1987, p. 334.
13. B. D. Ralph and A. S. Michael, *Goodness-of-fit Techniques*, Marcel Dekker, Inc., New York, 1986.
14. J. H. Mathews, *Numerical Methods for Computer Science, Engineering, and Mathematics*, Prentice-Hall, Inc., New Jersey, 1987, pp. 238–249.
15. Ref. 4, pp. 231–232.
16. J. Long, L. Jones and P. Chen, *In Vitro Wettability of Hydrogel Contact Lenses*, submitted for publication.
17. J. M. Ortega and W. C. Rheinboldt, *Iterative Solution of Nonlinear Equations in Several Variables*, Academic Press, New York, 1970.